Available online at www.sciencedirect.com
SCIENCE DIRECT®
International Journal of Heat and Mass Transfer 48 (2005) 3995–4009
International Journal of HEAT and MASS TRANSFER
www.elsevier.com/locate/ijhmt

Developing fluid flow and heat transfer in a channel partially filled with porous medium

Tien-Chien Jen *, T.Z. Yan

Mechanical Engineering Department, University of Wisconsin at Milwaukee, Milwaukee, WI 53211, United States

Received 24 August 2004; received in revised form 15 April 2005

Abstract

A three-dimensional computational model is developed to analyze fluid flow in a channel partially filled with porous medium. In order to understand the developing fluid flow and heat transfer mechanisms inside the channel partially filled with porous medium, the conventional Navier–Stokes equations for gas channel, and volume-averaged Navier–Stokes equations for porous medium layer are adopted individually in this study. Conservation of mass, momentum and energy equations are solved numerically in a coupled gas and porous media domain along a channel using the vorticity–velocity method with power law scheme. Detailed development of axial velocity, secondary flow and temperature field at various axial positions in the entrance region are presented. The friction factor and Nusselt number are presented as a function of axial position, and the effects of the size of porous media inside the channel partially filled with porous medium are also analyzed in the present study.

Keywords: Porous medium; Numerical analysis

1. Introduction

Fluid flow and heat transfer in a channel partially filled with porous medium are important in many engineering applications such as thermal insulation, water movement geothermal reservoirs, grain storage, solar collector, food processing, fuel cells and many other electrochemical systems. In order to optimize the design considerations for various specific applications, it is necessary to better understand fundamental mechanisms in the fluid flow and thermal transport. The influence of velocity, temperature, and pressure distributions in a channel partially filled with porous medium must be mapped into enabling the selection of specific operation parameters for any applications. One of the important applications, for example, is for the heat transfer, fluid flow and mass transport analyses on the membrane electrode assembly (MEA) and gas flow channels in the fuel cell. It is worth noting that fuel cells offer the potential of ultra-low emissions combined with high efficiency power output. Recent rapid advances in fuel cell technology have resulted in a vast increase in fuel cell research and development directed towards wide spread applications, such as electric powered vehicle, wireless communications [1] and stationary power supply [2]. A typical proton exchange membrane (PEM) fuel cell consists of a gas channel; porous media gas diffuser, porous catalyst layer and membrane. It is therefore necessary to analyze

* Corresponding author. Tel.: +414 229 2307; fax: +414 229 6958.
E-mail address: jen@cae.uwm.edu (T.-C. Jen).

0017-9310/$ - see front matter © 2005 Published by Elsevier Ltd.
doi:10.1016/j.ijheatmasstransfer.2005.04.021

Nomenclature

A	cross-section area, cm^2
Da	Darcy number, κ/D_e^2
D_e	hydraulic diameter, $4A/S'$, cm
Pr	Prandtl number
R	gas constant, J/mol K
Re	Reynolds number
S	porous layer thickness ratio
S'	perimeter
T	temperature, K
T_m	mean temperature, K
a	channel width, cm
b	porous media thickness, cm
k_{gr}	porous media conductivity
k_{gas}	fluid gas conductivity
u, v, w	velocity in x, y, z-direction, cm/s
p	pressure, Pa

Greek symbols

ε	porosity, 0.5
ρ	density, g/cm^3
κ	permeability, cm^2
ν	kinematic viscosity, cm^2/s
μ	dynamic viscosity, g/cm s
ζ	vorticity

Superscript

$-$	non-dimensional variable

Subscripts

i	inlet
eff	effective

the fluid flow, heat transfer and mass transport inside of the fuel cell to further improve the performance of the fuel cell [3,4].

A general theory and numerical techniques for flow field and heat transfer were developed and simulated in a rectangular duct without porous media have been studied by Clark and Kays [5]. They used numerical method to evaluate Nu for $\alpha^* = 0$, 0.25, 1/3, 0.5, 1/1.4, and using a $10 \times 10\alpha^*$ grid. Here α^* denotes aspect ratio. Miles and Shih [6] refined the calculations by employing a denser grid of $40 \times 40\alpha^*$. Schmidt and Newell [7] used finite difference method to calculate the flow and temperature fields, and compute the Nusselt number. For a porous media channel, most existing related studies on convection heat transfer in composite system were focused on the problem of natural convection [8–17]. There have been very few investigations on the interaction of forced convection on fluid layer and porous layer in a composite system. This type of problem was first investigated by Beavers and Joseph [18]. They presented an empirically based correlation for the velocity gradient at the interface in terms of the velocity in the fluid layer and porous media region. Later, this problem was studied by Vafai and Thiyagaraja [19]. They analytically studied the fluid flow and heat transfer for three types of interfaces: interface between two different porous media, the interface separating a porous medium from a fluid region and the interface between a porous medium and impermeable medium. They obtained an analytical solution based on matched asymptotic expansions for velocity and temperature distribution. Vafai and Kim [20] revisited the same problem and presented an exact solution for the fluid flow without any approximation. In their study, the shear stress in the fluid and the porous medium were taken to be equal at the interface region. The exact solution for the temperature distribution is solved by matched asymptotic double expansion perturbation solution of Vafai and Kim [20].

More recently, Ochoa-Tapia and Whitaker [21] presented a hybrid interface condition. They assumed a jump, which is proportional to the permeability of the porous medium, on the shear stress at the interface region. Ochoa-Tapia and Whitaker [22] also proposed a hybrid interface condition for the heat transfer process, in which they introduce a jump condition to account for possible excess in the heat flux at the interface. Very recently, Alazmi and Vafai [23] critically examined the differences in the fluid flow and heat transfer characteristics due to different interface conditions. In their study, five primary categories for interface conditions for the fluid flow and four primary forms of interface conditions for the heat transfer between a porous medium and a fluid layer were considered.

To date, however, most of these existing related studies on convection in composite systems of porous media were focused on the interface boundaries and/or natural convection in an enclosure [24–30]. To the best of the authors' knowledge, there have not been any investigations on the forced convection in a composite channel with porous medium in the open literature.

The present work constitutes the development of a three-dimensional (3-D) model and the simulation using a novel numerical technique to analyze the general heat convection and fluid flow in a channel partially filled with porous medium. In this study, instead of multiple domains, in which requires the specification of the interface conditions [23], we used a single-domain CFD formulation for porous medium and fluid layer. Using this

approach, the boundary conditions for both fluid flow and heat transfer at the interface of the porous media are automatically coupled. This eliminates the needs to specify the interface boundary condition between porous medium and fluid layer. A vorticity–velocity with power law scheme [31] was employed to solve the flow pattern including the axial velocity, secondary flows, and temperature distribution in various cross sections. The friction factors and Nusselt number variations along the composite porous channel are also shown and discussed in details.

2. Model description and assumption

Consider a steady, laminar, incompressible, developing flow with constant properties in a square duct ($a \times a$), inside the duct a porous media with thickness b is depicted in Fig. 1. The axial diffusion, viscous dissipation, compression work and buoyancy are assumed negligible. Assuming strong axial flows and moderate secondary velocities inside the channels, the axial diffusion and gravitational force are neglected. It is further assumed that the fluid flow in the channel is at uniform speed U_i and constant temperature T_0. Note that for the gas channel, the geometry of channel is rectangular with a dimension of $a \times (a-b)$. The temperatures at channel walls are assumed to be at constant T_w.

The fluid flow in the channel is described by the conventional Navier–Stokes equations. The axial and cross-sectional pressure gradients may be decoupled by making the usual parabolic assumption [32]. A modified pressure P may be defined as

$$P(X,Y,Z) = p(Z) + p^*(X,Y), \tag{1}$$

where $p(Z)$ is the pressure over the cross section at each axial location, and $p^*(X,Y)$ is the pressure variation in the X- and Y-direction, which drives the secondary flows. Pressure gradient for axial direction can be expressed as

$$\frac{\partial P}{\partial Z} = \frac{\partial p}{\partial Z} + \frac{\partial p^*}{\partial Z}, \tag{2}$$

where $\frac{\partial p}{\partial Z} \gg \frac{\partial p^*}{\partial Z}$ is due to the parabolic assumption.

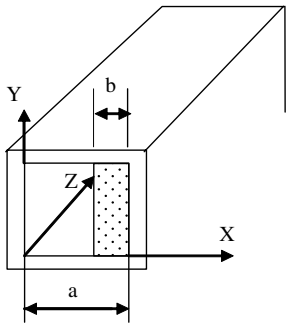

Fig. 1. The model geometry.

So, the axial pressure gradient can be written as

$$\frac{\partial P}{\partial Z} = \frac{\partial p}{\partial Z} = f(Z), \tag{3}$$

$$\frac{\partial P}{\partial X} = \frac{\partial p^*}{\partial X}, \tag{4}$$

$$\frac{\partial P}{\partial Y} = \frac{\partial p^*}{\partial Y}. \tag{5}$$

2.1. Governing equations

Fluid flow and heat transfer in a channel partially filled with porous medium is described by conservation of mass, momentum, and energy. Particular forms of transport equations in porous media maybe derived in terms of macroscopic variables. The macroscopic velocity in porous medium is provided by the volume-averaged Navier–Stokes equations [19]. These equations are a generalized form of Darcy's law.

The following dimensionless variables and parameters are introduced to non-dimensionalize governing equations:

$$\begin{aligned} &D_e = \frac{4A}{S'}, \quad \bar{u} = \frac{U}{U_i}, \quad \bar{v} = \frac{V}{U_i}, \quad \bar{w} = \frac{W}{U_i}, \\ &\bar{x} = \frac{X}{D_e}, \quad \bar{y} = \frac{Y}{D_e}, \quad \bar{z} = \frac{Z}{D_e Re}, \quad \bar{p} = \frac{P - P_i}{\rho_i U_i^2}, \\ &Re = \frac{\rho_i U_i D_e}{\mu}, \quad D_a = \frac{\kappa}{D_e^2}, \quad \overline{T} = \frac{T - T_w}{T_o - T_w}. \end{aligned} \tag{6}$$

With the same assumptions mentioned above, the model equations can be written in general form for both gas channel and porous media, as

$$\frac{\partial \bar{u}}{\partial \bar{x}} + \frac{\partial \bar{v}}{\partial \bar{y}} + \frac{\partial \bar{w}}{\partial \bar{z}} = 0, \tag{7}$$

$$\begin{aligned} &Re\frac{1}{\varepsilon^2}\left(\bar{u}\frac{\partial \bar{u}}{\partial \bar{x}} + \bar{v}\frac{\partial \bar{u}}{\partial \bar{y}} + \bar{w}\frac{\partial \bar{u}}{\partial \bar{z}}\right) \\ &\quad = -\frac{\partial \bar{p}}{\partial \bar{x}} + \frac{1}{\varepsilon}\left(\frac{\partial^2 \bar{u}}{\partial \bar{x}^2} + \frac{\partial \bar{u}^2}{\partial \bar{y}^2}\right) - \frac{1}{D_a}\bar{u}, \end{aligned} \tag{8}$$

$$\begin{aligned} &Re\frac{1}{\varepsilon^2}\left(\bar{u}\frac{\partial \bar{v}}{\partial \bar{x}} + \bar{v}\frac{\partial \bar{v}}{\partial \bar{y}} + \bar{w}\frac{\partial \bar{v}}{\partial \bar{z}}\right) \\ &\quad = -\frac{\partial \bar{p}}{\partial \bar{y}} + \frac{1}{\varepsilon}\left(\frac{\partial^2 \bar{v}}{\partial \bar{x}^2} + \frac{\partial \bar{v}^2}{\partial \bar{y}^2}\right) - \frac{1}{D_a}\bar{v}, \end{aligned} \tag{9}$$

$$\begin{aligned} &Re\frac{1}{\varepsilon^2}\left(\bar{u}\frac{\partial \bar{w}}{\partial \bar{x}} + \bar{v}\frac{\partial \bar{w}}{\partial \bar{y}} + \bar{w}\frac{\partial \bar{w}}{\partial \bar{z}}\right) \\ &\quad = -f(\bar{z}) + \frac{1}{\varepsilon}\left(\frac{\partial^2 \bar{w}}{\partial \bar{x}^2} + \frac{\partial^2 \bar{w}}{\partial \bar{y}^2}\right) - \frac{1}{D_a}\bar{w}, \end{aligned} \tag{10}$$

$$PrRe\frac{1}{\varepsilon}\left(\bar{u}\frac{\partial \overline{T}}{\partial \bar{x}} + \bar{v}\frac{\partial \overline{T}}{\partial \bar{y}} + \bar{w}\frac{\partial \overline{T}}{\partial \bar{z}}\right) = \left(\frac{\partial^2 \overline{T}}{\partial \bar{x}^2} + \frac{\partial^2 \overline{T}}{\partial \bar{y}^2}\right), \tag{11}$$

where Da is Darcy number. κ/D_e^2, where D_e is the hydraulic diameter, and κ is the permeability of the porous media. ε is the porosity. For the region of regular fluid channels, the value of ε is equal to 1. Note that for the region of the channel where there is no porous media, κ is chosen to be a large number that forces the last term of the momentum equations (Eqs. (8)–(10)) drop to zero.

The Prandtl number Pr for porous media is defined as

$$Pr = \frac{c_p \mu}{k_{\text{eff}}}. \tag{12}$$

Here k_{eff} is the effective macroscopic thermal conductivity, which is given as follows [33]:

$$k_{\text{eff}} = -2k_{\text{gr}} + \frac{1}{\dfrac{\varepsilon}{2k_{\text{gr}} + k_{\text{liq}}} + \dfrac{1-\varepsilon}{3k_{\text{gr}}}}, \tag{13}$$

where k_{gr} is porous media conductivity, and k_{liq} is fluid gas conductivity.

2.2. Vorticity–velocity formulations

A vorticity–velocity method was first developed for two-dimensional fluid flow simulations by several researchers, such as Farouk and Fusegi [34] and Orlandi [35]. This formulation was then extended directly to three-dimensional parabolic flow as shown in Chou and Hwang [36], Jen and Lavine [37] and Jen et al. [31]. This method removes the difficulties that encountered in the vorticity-stream function approach, which can only be used in two-dimensional flow. This approach has a superior advantage over the commonly used primitive variables method that the pressure terms are eliminated from the formulations. This method is therefore adopted in the present study.

In this approach, the axial vorticity function is defined as

$$\zeta = \frac{\partial \bar{u}}{\partial \bar{y}} - \frac{\partial \bar{v}}{\partial \bar{x}}. \tag{14}$$

Applying to continuity equation yields

$$\nabla^2 \bar{u} = \frac{\partial \zeta}{\partial \bar{y}} - \frac{\partial^2 \bar{w}}{\partial \bar{x} \partial \bar{z}}, \tag{15}$$

$$\nabla^2 \bar{v} = -\frac{\partial \zeta}{\partial \bar{x}} - \frac{\partial^2 \bar{w}}{\partial \bar{y} \partial \bar{z}}. \tag{16}$$

Cross differentiation of x and y momentum equations to eliminate pressure terms yields

$$Re\frac{1}{\varepsilon}\left(\bar{u}\frac{\partial \zeta}{\partial \bar{x}} + \bar{v}\frac{\partial \zeta}{\partial \bar{y}} + \bar{w}\frac{\partial \zeta}{\partial \bar{z}} + \zeta\left(\frac{\partial \bar{u}}{\partial \bar{x}} + \frac{\partial \bar{v}}{\partial \bar{y}}\right) + \left(\frac{\partial \bar{w}}{\partial \bar{y}}\frac{\partial \bar{u}}{\partial \bar{z}} - \frac{\partial \bar{w}}{\partial \bar{x}}\frac{\partial \bar{v}}{\partial \bar{z}}\right)\right) + \frac{\varepsilon D_e^2}{k}\zeta = \left(\frac{\partial^2 \zeta}{\partial \bar{x}^2} + \frac{\partial^2 \zeta}{\partial \bar{y}^2}\right). \tag{17}$$

An additional constraint, which is used to determine $f(\bar{z})$ is that global mass conservation must be satisfied at each cross-section. Defining a different non-dimensional axial velocity, w_t, for convenience, this constraint can be expressed as

$$\bar{w}_t = \int_0^1 \int_0^1 w_t \, \mathrm{d}\bar{x} \, \mathrm{d}\bar{y} = 1.0, \tag{18}$$

where $w_t = \bar{w} Re$.

The boundary conditions can be written as follows:

$\bar{u} = \bar{v} = \bar{w} = \overline{T} = 0$ at walls
$\bar{u} = \bar{v} = \zeta = 0$, $w_t = \overline{T} = 1$ at $\bar{z} = 0$ for fluid channel
$\bar{u} = \bar{v} = \zeta = 0$, $w_t = \overline{T} = 1$ at $\bar{z} = 0$ for porous media.

Once the developing velocity and temperature fields along the axial direction are calculated from the above equations, the computation of local friction factor and the Nusselt number are of practical interest. The local friction factor and Nusselt number can be written based on the velocity gradient along an axial length $\mathrm{d}\bar{z}$ and the temperature gradient at the wall and the interface of the porous media. The results are

$$fRe = -\frac{1}{2}\int_0^1 \int_0^1 \frac{\partial w_t^2}{\partial \bar{z}} \, \mathrm{d}\bar{x} \, \mathrm{d}\bar{y}. \tag{19}$$

The local Nusselt numbers are

$$Nu = \frac{1}{\overline{T}_{\text{m}}}\frac{P_r}{S'}\int_0^1 \int_0^1 \frac{\partial w_t \overline{T}}{\partial \bar{z}} \, \mathrm{d}\bar{x} \, \mathrm{d}\bar{y}, \tag{20}$$

where S' is the perimeter of the duct. The quantity $\overline{T}_{\text{m}}$ is defined as

$$\overline{T}_{\text{m}} = \frac{T_{\text{m}} - T_{\text{w}}}{T_{\text{in}} - T_{\text{w}}} = \int_0^1 \int_0^1 w_t \overline{T} \, \mathrm{d}\bar{x} \, \mathrm{d}\bar{y}, \tag{21}$$

where T_{m} is mean temperature.

3. Method of solution

The governing equations are solved numerically by vorticity–velocity method for three-dimensional parabolic flow along with power-law scheme [38]. A single domain approach is used in this study since the governing equations in liquid channel and porous media are very similar; the only differences are from either additional terms or the parameters. Note that with this approach, the interface conditions can be satisfied automatically without any further treatment at the interface. The procedure is as follows:

1. The initial values of $\bar{u}$, $\bar{v}$, ζ are assigned to be zero at the entrance, $\bar{z} = 0$. Inlet axial velocity and temperature are assigned to be uniform at the entrance of liquid channel. The values of the entrance of porous media region are set to be zero.

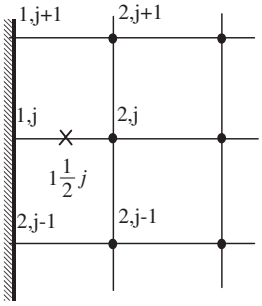

Fig. 2. Vorticity at the wall.

2. The boundary vorticity can be evaluated with the following expression [36] (Fig. 2):

$$\zeta_{1,j} = \frac{1}{2\Delta\bar{y}}(\bar{u}_{2,j+1} - \bar{u}_{2,j-1}) - \frac{2\bar{v}_{2,j}}{\Delta\bar{x}} + \zeta_{2,j}. \tag{22}$$

3. Discretize equations (10), (15), (16) and (17) using power-law scheme. And the values of $\frac{\partial\bar{w}}{\partial\bar{x}}$, $\frac{\partial\bar{w}}{\partial\bar{y}}$, $\frac{\partial\bar{u}}{\partial\bar{x}}$, and $\frac{\partial\bar{v}}{\partial\bar{y}}$ are discretized using central differencing at each grid point. The values of $\frac{\partial\bar{u}}{\partial\bar{z}}$ and $\frac{\partial\bar{v}}{\partial\bar{z}}$ are computed by two- points backward differencing. The values of $\frac{\partial^2\bar{w}}{\partial\bar{x}\partial\bar{z}}$, $\frac{\partial^2\bar{w}}{\partial\bar{y}\partial\bar{z}}$, $\frac{\partial\bar{\zeta}}{\partial\bar{x}}$ and $\frac{\partial\bar{\zeta}}{\partial\bar{y}}$ are calculated by using backward differences axially and central differences in the transverse directions.
4. Solve Eq. (17) first to obtain vorticity ζ. Then solve elliptic-type equations (15) and (16) iteratively using known value of ζ until the following convergence criterion has to be satisfied for velocity u and v.

$$\varepsilon' = \frac{\max\left|\bar{u}_{i,j}^{n+1} - \bar{u}_{i,j}^{n}\right|}{\max\left|\bar{u}_{i,j}^{n+1}\right|} \leqslant 10^{-5}, \tag{23}$$

where n is the nth iteration step.

After getting ζ, $\bar{u}$ and $\bar{v}$, Eq. (10) can be solved with an initial guess value of $f(\bar{z})$. The new value of $\bar{w}$ has to be satisfied relationship (18). Otherwise the initial guess value of $f(\bar{z})$ has to be regulated until it meets the requirement of constant flow rate.

5. Repeat steps 2–4 until both convergence criterions is satisfied.
6. With the solutions of $\bar{u}$, $\bar{v}$, and $\bar{w}$, Eq. (11) can be solved iteratively for the interior temperature subject to the various boundary conditions. This step is repeated until the following convergence criterion is satisfied:

$$\varepsilon' = \frac{\max\left|\overline{T}_{i,j}^{m+1} - \overline{T}_{i,j}^{m}\right|}{\max\left|\overline{T}_{i,j}^{m+1}\right|} \leqslant 10^{-6},$$

where m is the mth iteration of the step 6.
7. Repeat steps 2–6 at the next axial location until the final location is reached.
8. The peripherally average friction factor and Nusselt numbers are determined from Eqs. (19) and (20).

4. Computational tests and details

Uniform mesh sizes of 31×31, 61×61, 91×91 are used for the grid independence tests the cross-sectional region in the composite square channel. The axial step size $\Delta\bar{z}$ was varied from 10^{-5} near the channel entrance to about 2.5×10^{-3} near the fully developed region. The grid independence tests in axial direction have also been performed for smaller marching steps starting at $\Delta\bar{z} = 10^{-6}$. For the grid sizes of 61×61 and 91×91, the changes in predicted friction coefficient and Nusselt number are less than 1% at the same flow condition. The axial velocities both in porous media and liquid channel are less than 0.5% in the same location with same flow condition. As an additional verification of the computational procedure, the hydrodynamically developing flow was calculated on non-porous square channel (let porosity equals 1 and permeability equals a very large number). The results were compared favorably with Shah and London [39]. It was found that the apparent friction factors were found to agree within 1% at all axial

Table 1
Computational test

Grids		31×31	61×61	91×91
$\bar{z} = 0.0008$	w at $\bar{x}=0.2$, $\bar{y}=0.2$	1.644448	1.642347	1.639776
	w at $\bar{x}=0.9$, $\bar{y}=0.9$	0.039596	0.039425	0.039173
	fRe	158.6313	158.34203	158.12545
	Nu	32.40624	32.12936	32.31502
$\bar{z} = 0.02$	w at $\bar{x}=0.2$, $\bar{y}=0.2$	2.142195	2.107892	2.106438
	w at $\bar{x}=0.9$, $\bar{y}=0.9$	0.0031162	0.0030582	0.0030491
	fRe	38.18202	38.03056	38.02912
	Nu	2.77174	2.72743	2.725643

locations. Base on the above observations, a 91×91 grid size and an initial step size of $\Delta\bar{z} = 10^{-5}$ is used throughout this study (Table 1).

5. Results and discussion

In the present study, we consider a square composite channel. This composite channel consists of two regions, one region is fully occupied by fluid layer, and a porous media layer, as shown in Fig. 1, occupies the other region. In most of the cases studied, Reynolds number is chosen to be 100. The effect of Reynolds number on the friction factors and Nusselt numbers will also be presented. The typical axial velocity profiles development, the secondary flow patterns, and the isotherm maps in different cross-sections are demonstrated in this section. The effect of the thickness ratio of the porous layers, $\varepsilon = 0.5$, and Darcy numbers are also examined. Finally, the axial variations of the friction factors and Nusselt numbers with different porous media layer thickness are presented.

5.1. Axial velocity development

The profile of the axial velocity near the entrance at $\bar{z} = 0.0008$ with a porous ratio 2/3 and Darcy number equals 10^{-5} is shown in Fig. 3a and b. It can be seen that the axial velocity in porous layer is very small compared with axial velocity in fluid layer. Due to the strong resistance of the porous layer, fluid squeezed out from the porous medium to fluid layer, which is similar to a blowing boundary condition. The fluid comes out from porous medium pushes the peak of the velocity to left side. Therefore, the axial velocity profiles are not symmetric in the fluid layer tube near the entrance region (i.e., $\bar{z} = 0.0008$). Fig. 3a shows the axial velocity profiles at several different $\bar{y}$ locations. Near bottom the wall ($\bar{y} = 0.05$), the strong secondary flow moving downward causes the large velocity gradient near the fluid layer and porous media interface. However, at $\bar{y} = 0.133$ the axial velocity profile has a very obviously s-shape distortion. This is a location, where there exists a strong vortex. This vortex is acting counter-clockwise, thus distorts the axial velocity into a s-shape. The maximum velocity is pushed further toward the sidewall. Fig. 3b shows the velocity profiles across the y-direction with several different x-locations at $\bar{z} = 0.0008$. It can be seen very clear that there are two peak velocities occurs in each x location, except at $\bar{x} = 0.05$, which is very close to the side wall where the secondary flow strength is fairly weak. These double peak velocities with a minor peak near the center are caused by the generation of a pair of counter-rotating vortices in the fluid channel. It is worth pointing out that for the velocity profile at $\bar{x} = 0.32$, a central dip in velocity at the minor peak center was observed. This is due to the generation of a second pair of vortex at the center of the fluid layer near the porous media, which is the set-in of the secondary instability. This phenomenon will be described in more details later. Fig. 3c and d illustrates the axial velocity profiles at the same location of $\bar{z} = 0.0008$ with porous layer ratio reduced to 1/2. The velocity profiles are quite similar to the cases shown in Fig. 3a and b, except that the maximum velocity decreases from 4.8 to 3.1. This is mainly because larger cross-sectional area in the fluid channel for smaller porous layer ratio, which results in smaller maximum velocity in the fluid channel. The double peaks (with minor peak) velocity profiles can be seen clearly in Fig. 3d. Note that no clear velocity dip near the center was observed; this is because the second pair vortex is weak when the porous layer ratio is decreased. Fig. 3e and f depicts the axial velocity profiles at different x and y locations at cross section $\bar{z} = 0.0008$ when the porous layer thickness ratio decreases to 1/3. It can be seen from the figures that the velocity perturbations due to the vortices are smaller than those in larger porous layer ratios (see Fig. 3a–d). This is due to the delay of the development of the second pair vortex. A weak twin peak axial velocity profile at $\bar{x} = 0.492$ can be seen in Fig. 3f, which indicates the onset of the first pair of vortices. Figs. 4 and 5 illustrate the effect of porous ratios and Darcy numbers on the axial y-velocity profiles in the fully developed flow regime. In Fig. 4, at the axial location of $\bar{z} = 0.1$ with a porous layer ratio of 1/2 and $Da = 10^{-5}$, all the velocity profiles have reached fully developed condition. The maximum velocity in the fluid channel, as observed, reaches approximately 3.8. In the porous layer, it is seen that the axial velocity is very small. This is due to the very small permeability in the porous layer (i.e., $Da = 10^{-5}$). Fig. 5 depicts the axial y-velocity profiles at $\bar{z} = 0.05$ with a porous layer ratio of 3/4 and $Da = 2.5 \times 10^{-4}$. It is observed that a fully developed flow condition has been established in the fluid channel, with a maximum velocity around 5.5. Again, this increase in maximum velocity is simply due to the larger porous layer ratio in the channel (smaller fluid layer ratio). This result is very similar to the result of the exact solution of Vafai and Kim [20]. Due to their assumption of the infinite porous medium and limit fluid layer, the maximum velocity in the fluid layer is much higher than that of our composite channel flow. It is also interesting to see that the axial velocity is very uniform across the porous layer, with a magnitude of 0.25. Note that the velocity magnitude in the porous layer is no longer small as that in Fig. 4. This is due to larger porosity in this case (i.e., $Da = 2.5 \times 10^{-4}$). These results are also consistent with Tong and Sharatchandra's results for porous plates flow [40].

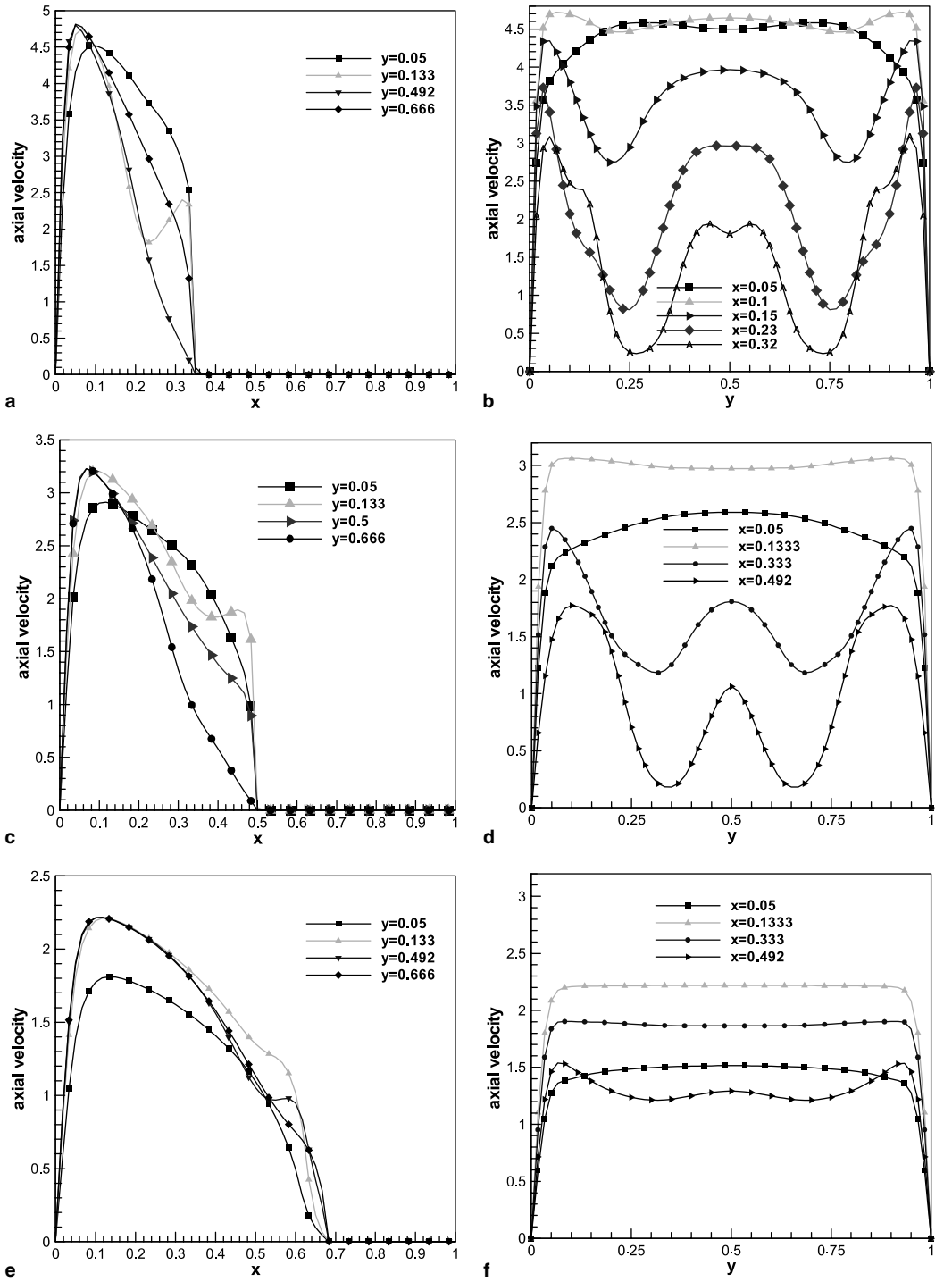

Fig. 3. (a) Axial velocity at $\bar{z} = 0.0008$ (2/3 porous, $Da = 10^{-5}$). (b) Axial velocity at $\bar{z} = 0.0008$ (2/3 porous, $Da = 10^{-5}$). (c) Axial velocity at $\bar{z} = 0.0008$ (1/2 porous, $Da = 10^{-5}$). (d) Axial velocity at $\bar{z} = 0.0008$ (1/2 porous, $Da = 10^{-5}$). (e) Axial velocity at $\bar{z} = 0.0008$ (1/3 porous, $Da = 10^{-5}$). (f) Axial velocity at $\bar{z} = 0.0008$ (1/3 porous, $Da = 10^{-5}$).

Fig. 6 displays the fully developed axial velocity profiles at $\bar{y} = 0.5$ compared with Sung's et al. [41] and Tong and Sharatchandra's [40] results of flat plates with porous insert (i.e., two-dimensional cases). It is observed

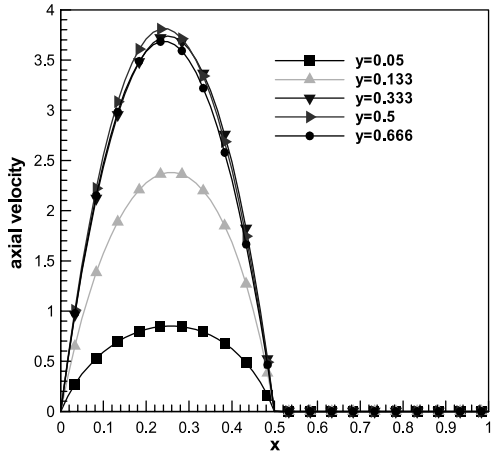

Fig. 4. Axial velocity at $\bar{z} = 0.1$ (1/2 porous, $Da = 10^{-5}$).

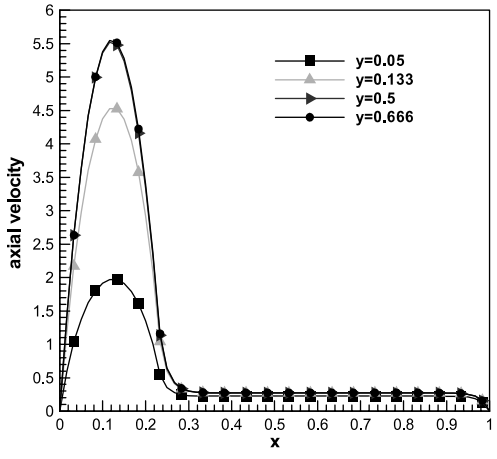

Fig. 5. Axial velocity at $\bar{z} = 0.05$ (3/4 porous, $Da = 2.5 \times 10^{-4}$).

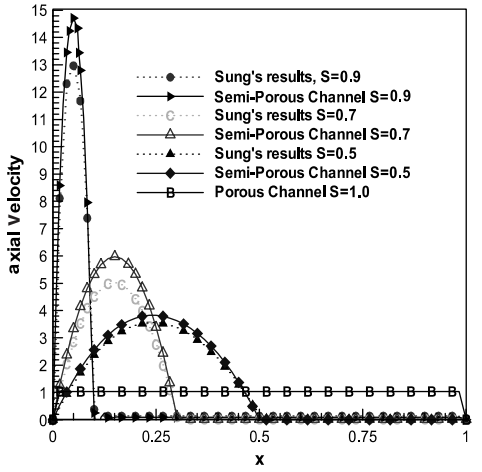

Fig. 6. Axial velocity at $\bar{y} = 0.5$, ($Re = 100$, $Da = 2.5 \times 10^{-5}$).

the axial velocity profiles are very similar, except the peak velocity of the composite channel is higher than that of flow in the flat plates with porous medium insert. This result seems plausible since the maximum velocity in a rectangular channel should be higher than the maximum velocity for flat plates flow. The effect of porous ratio in the channel with fixed Re ($Re = 100$) and Da ($Da = 2.5 \times 10^{-5}$) is also exhibited. When the porous ratio increases, the fluid flow has been squeezed toward the fluid layer due to the existence of the porous layer, thus the maximum velocity increases. It is also worth noting that the velocity gradient is also increased, this in turn causes the increase in pressure drop.

Fig. 7a–d shows the isovel patterns at location $\bar{z} = 0.008$ for four different porous ratios, $S = 5/6$, 2/3, 1/2 and 1/3, respectively. This axial location is chosen to show the effect of porous ratios in the early flow-developing region. It can be seen from the figures that strong axial velocity disturbances occur near the interface between fluid layer and porous layer. This is due to the effect of transverse flow blowing that squeezed the fluid out of the porous channel. This blowing causes the onset of two strong counter-rotating vortices in the fluid layer. A very intense velocity gradient near the side wall can be observed, this is again due to the blowing effect of the porous layer pushes the fluid to the side wall. The isovel pattern also shows high velocity gradients near the top and bottom walls, which is due the flow returning from the top and bottom wall. This is similar to the case as Ekman suction in rotating flow field [45,46].

It is also interesting to note that there exists three strong isolated high velocity peaks when the porous ratio is greater than 1/2. This can also be seen in Fig. 3b and d.

Fig. 7c, e and f demonstrates the axial variations of the isovel patterns in the developing flow region for porous ratio of 1/2. Fig. 7e shows the isovel pattern at location $\bar{z} = 0.0008$, which is very close to inlet. Therefore, a large dense uniform isovel contours can be seen near the solid wall, which suggests very large axial velocity gradients. The strong twisted axial velocity is observed near the interface of the porous media. This is due to the strong flow blowing out of the porous layer. It can also be seen that the effect of blowing has not affected the axial velocity near the sidewall. When the axial location moves further downstream to $\bar{z} = 0.008$ (Fig. 7c), it can be seen that the effect of transverse blowing due to the porous layer has been penetrated further into the fluid layer and form three isolated peak axial velocity regions. Finally, in fully developed region ($\bar{z} = 0.1$), the axial velocity approaches parabolic flow as shown in Fig. 7f.

It is worth noting that almost all the analyses reported earlier, such as [42,43,41], were all confined to the fully developed region. The axial dependence, or

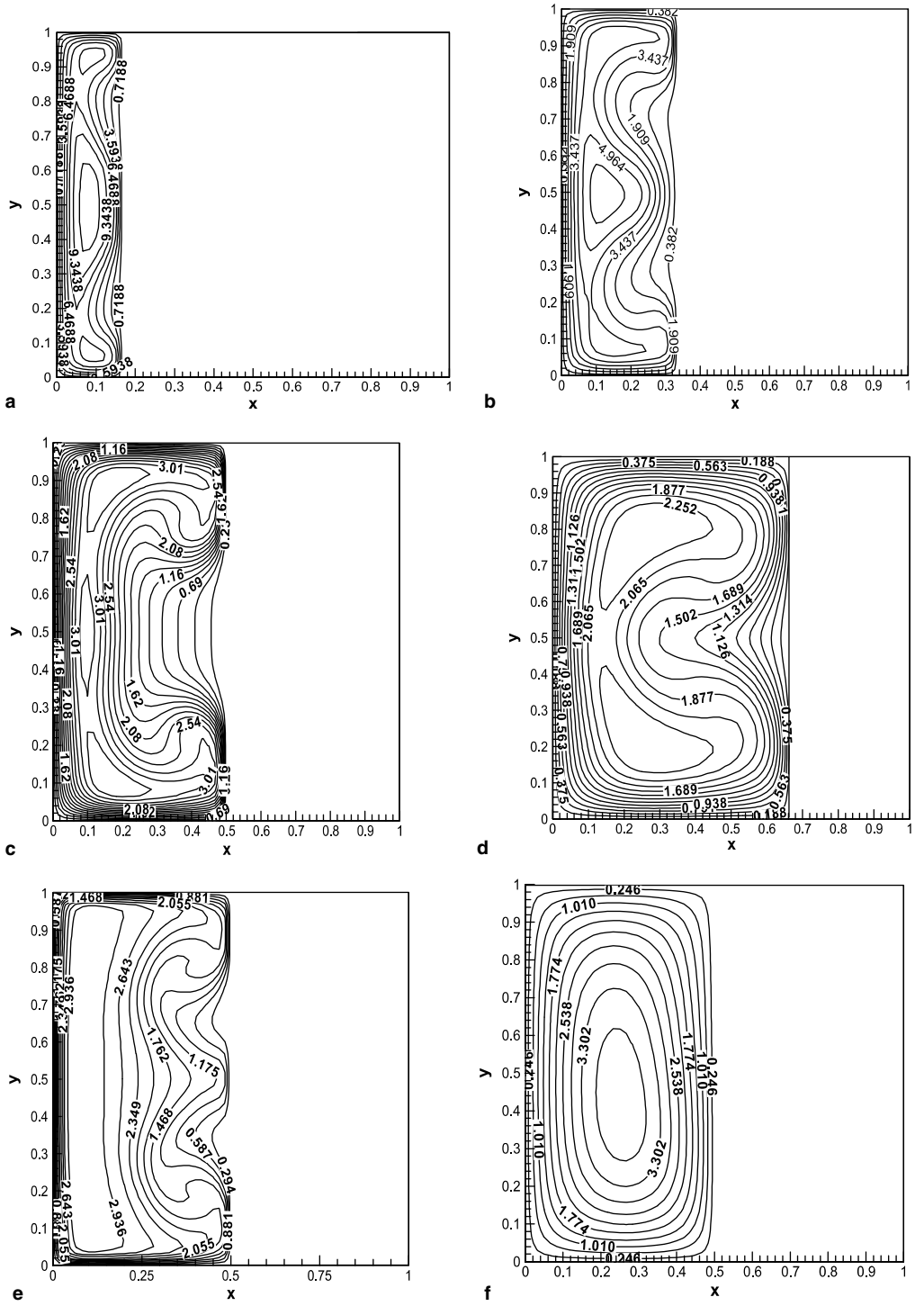

Fig. 7. (a) Isovel pattern at $\bar{z} = 0.008$ (5/6 porous, $Da = 10^{-5}$). (b) Isovel pattern at $\bar{z} = 0.008$ (2/3 porous, $Da = 10^{-5}$). (c) Isovel pattern at $\bar{z} = 0.008$ (1/2 porous, $Da = 10^{-5}$). (d) Isovel pattern at $\bar{z} = 0.008$ (1/3porous, $Da = 10^{-5}$). (e) Isovel pattern at $\bar{z} = 0.0008$ (1/2 porous, $Da = 10^{-5}$). (f) Isovel pattern at $\bar{z} = 0.1$ (1/2 porous, $Da = 10^{-5}$).

entrance effect, has never been investigated theoretically. The present calculation not only includes the entrance effect, but also reveals the generation of the second pair vortices in the fluid layer.

5.2. Secondary flow patterns

In the present study, information about the flow field developments are provided via vector plots of secondary flow. Fig. 8a–e shows the secondary flow patterns with different porous layer ratio at the location $\bar{z} = 0.0008$. Fig. 8a shows the secondary flow pattern in a fully porous channel. It is worth noting that there exist 4 axis-symmetric pairs for counter-rotating vortices in the fully porous channel. This secondary flow pattern is very much similar to turbulent secondary flows in a square duct, which were obtained earlier by Speziale [44]. However, these vortices are diminishing rapidly along the flow direction in the present simulation. Fig. 8b shows the secondary flow pattern of a channel with porous aspect ratio of 1/2. It is clearly seen that there exist two large vortices in fluid layer near the interface of the porous media layer with a pair of smaller vortices in porous media layer. This is due to the flow instability generated by the blowing effect of the porous layer. Since the pressure is lower in the fluid layer, the fluid in the high-pressure side porous layer is pushed out toward the fluid layer, which creates a blowing velocity. This velocity is distributed non-uniformly along the interface between fluid layer and the porous layer, which is squeezing out from the center due to higher-pressure difference in the center core region. This causes the generation of one pair of counter-rotating vortices. The second pair vortices were generated due to the local imbalance of the pressure force and the inertia force in the core region of the vicinity of the porous layer. This phenomenon is very similar to the roll-cell instabilities in pressure driven flow with rotation as shown in [45,46,37]. These vortices, especially in fluid layer, have a significant effect on the axial velocity profiles as discussed above. With the porous ratio decrease, the strength of the vortices in porous medium become comparable with the vortices in fluid layer in the entrance region, as shown in Fig. 8c and d. This is due to the decrease in strength of secondary flow for larger fluid layer. For further downstream at $\bar{z} = 0.008$, the secondary flow intensity in the porous layer diminishes dramatically as shown in Fig. 8e, with the porous layer ratio of 1/3. This is the only figure will be shown since similar results can be observed in other porous layer ratios. It can be explained that since the axial velocity decreases rapidly in the porous media layer, the magnitude of velocity in porous medium is much smaller than that in fluid layer. And the secondary flow is further weakened away from the inlet since the pressure distribution must extend to balance along the flow directions.

5.3. Temperature distribution

Fig. 9a–d demonstrates the isotherm maps with different porous ratio at the same axial location $\bar{z} = 0.0008$. It is observed that the temperature distribution is fairly uniform in porous media layer of the cross section. The physical mechanisms can be easily described; the heat transfer mechanism is pretty much dominated by heat conduction in porous media layer, and the very low velocity in porous media layer is unable to effectively transport the heat axially in the porous region. The heat convection is negligible compared with heat conduction in the porous layer. Thus, the heat transfer is mostly through transverse heat conduction from porous layer to the fluid layer region. In previous researches (e.g., [19]), a fixed thermal boundary condition is usually imposed in the porous-liquid layer interface. However, the observed isotherms vary significantly along the interface. This reveals that it may not be realistic to impose a fixed thermal boundary condition at the interface. It is also worth noting that the isotherms are slightly distorted toward to the porous "wall" and two axis-symmetric relatively high temperature cores are found near the interface. This is due to the effect of the counter-rotating vortices, which causes the non-uniform temperature distribution. Because of the blowing condition on the interface from porous layer to the fluid layer, it is observed that large temperature gradients are found near all the walls except near the interface. This can cause significant increase in the rate of heat transfer in these regions. Further downstream at $\bar{z} = 0.1$, which is near fully developed region, the thermal boundary layer becomes thicker and distributed more evenly at fluid layer; the cold temperature core is shrinking to the center of the fluid layer as shown in Fig. 9d.

5.4. Axial variations of friction factors

Fig. 10a shows that the fRe/fRe_0 varies along the axial direction for porous ratio $S = 5/6$ to 0, where fRe_0 is the fully developed value for the square channel without porous layer. In general, it can be seen from this figure that fRe increases with the porous ratio increase. This is because most fluid has been squeezed out of the porous layer; the shear stress at the walls attached to the porous layer becomes very small in comparison to the wall shear stress at the walls adjacent to the fluids layer. The pressure drop mostly depends on shear stress of solid wall and interface of the porous layer and the fluid layer. With the porous ratio increase, the velocity gradients in fluid layer increases due to larger volume flow rate, thus the friction factor ratio increases as the porous layer ratio increases as shown in Fig. 10a.

Fig. 10b shows the effect of porous ratio S on the friction factor ratio (fRe/fRe_0) in the fully developed region and also compares with the results of Sung's [41] plates flow with insert porous media layer. It can be seen that the present study predicts higher value for fully developed friction factor ratios than those of Sung's [41]. This

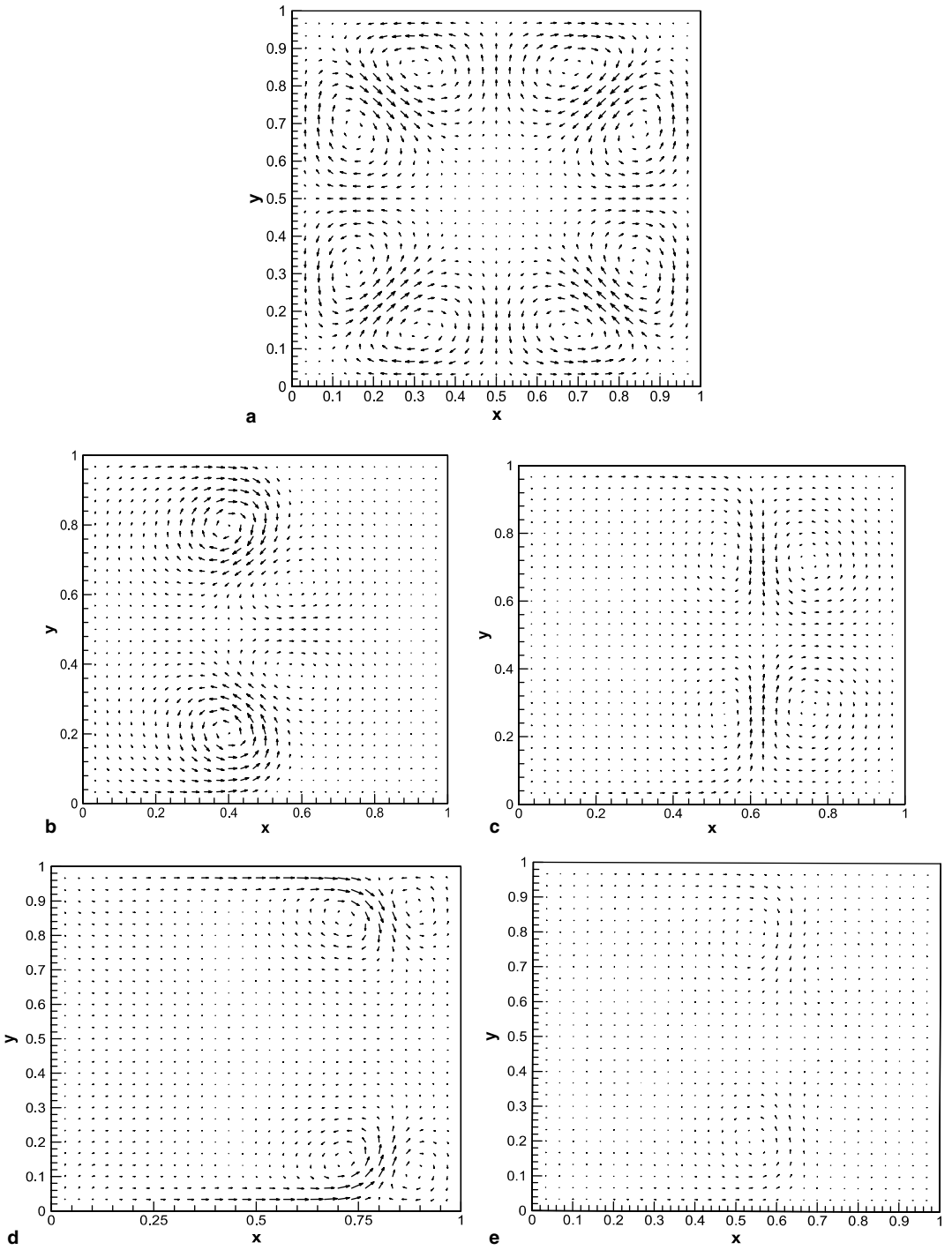

Fig. 8. (a) Secondary flow pattern of a full porous ratio at $\bar{z} = 0.0008$, $Da = 10^{-5}$. (b) Secondary flow pattern, 1/2 porous ratio at $\bar{z} = 0.0008$, $Da = 10^{-5}$. (c) Secondary flow pattern, 1/3 porous ratio at $\bar{z} = 0.0008$, $Da = 10^{-5}$. (d) Secondary flow pattern, 1/6 porous ratio at $\bar{z} = 0.0008$, $Da = 10^{-5}$. (e) Secondary flow pattern, 1/3 porous ratio at $\bar{z} = 0.0008$, $Da = 10^{-5}$.

may be due to the reason that our study is for a full three-dimensional analysis, while Sung's results [41] are for two-dimensional cases.

Fig. 10c shows the effect of Reynolds number on the axial variations of friction factor for porous ratio $S = 0.5$ and $Da = 10^{-5}$. It can be seen from the figure

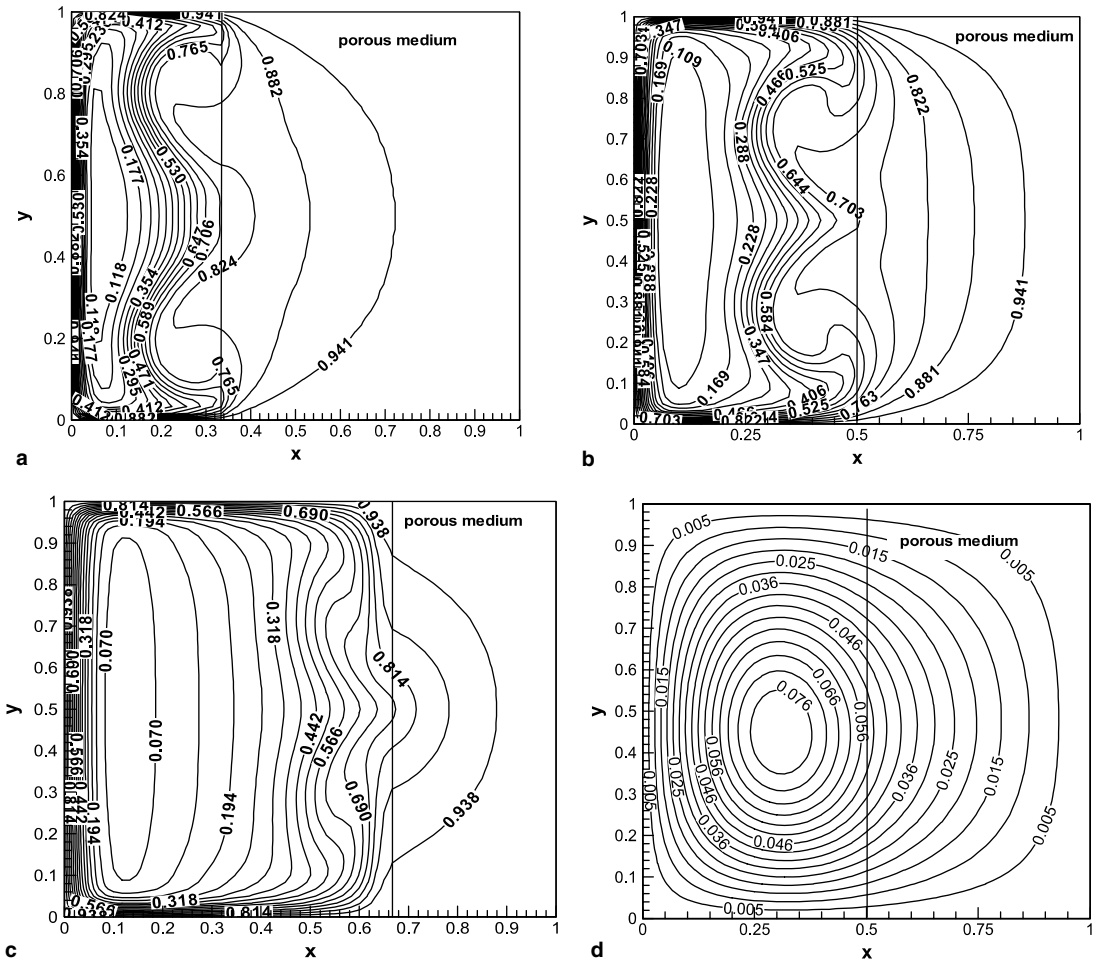

Fig. 9. (a) Isothermal pattern, 2/3 porous ratio at $\bar{z} = 0.0008$, $Da = 10^{-5}$. (b) Isothermal pattern, 1/2 porous ratio at $\bar{z} = 0.0008$, $Da = 10^{-5}$. (c) Isothermal pattern, 1/3 porous ratio at $\bar{z} = 0.0008$, $Da = 10^{-5}$. (d) Isothermal pattern, 1/2 porous ratio at $\bar{z} = 0.1$, $Da = 10^{-5}$.

that, the *fRe* is increased with increasing Reynolds number in all axial locations except very near the inlet (i.e., for $\bar{z} < 0.015$). This can be easily explained that larger the velocity in the fluid channel can result in larger wall shear stress near the channel's walls. The fully developed fRe increases from 68 to nearly 120 when the Reynolds number increases from 20 to 1000, and increases further to 162 when the Reynolds number reaches 2000.

5.5. Axial variation of Nusselt number for constant wall temperature

Fig. 11a illustrates the effect of Reynolds number on the axial variations of Nusselt number for porous ratio $S = 0.5$ and $Da = 10^{-5}$. Similarly, the Nusselt number is increased with increasing Reynolds number. This is not surprising since larger Reynolds number implies larger wall shear stress at the solid walls (and the interfaces between porous layer and fluid channel), thus creates larger temperature gradients in the corresponding areas. This larger temperature gradients result in larger heat transfer rate, and thus larger Nusselt number. It can be seen from the figure that the Nusselt number increases from 4.1 to 7.2 when the Reynolds number is increased from 20 to 1000, and is further increased to 12 when the Reynolds number becomes 2000. This shows a factor of 3 increases in Nusselt number.

Fig. 11b depicts the peripherally averaged Nusselt number variations in the axial direction for different porous ratio with $Re = 100$, $Pr = 0.7$, and $Da = 10^{-5}$. It is found that the axial Nusselt number increases with the porous ratio. These results are consistent with the friction factor ratios observed in Fig. 10a, since larger isotherms gradients are found near the walls adjacent to the fluid layer due to the larger velocity gradients. It can be seen from the figure that there exists several very

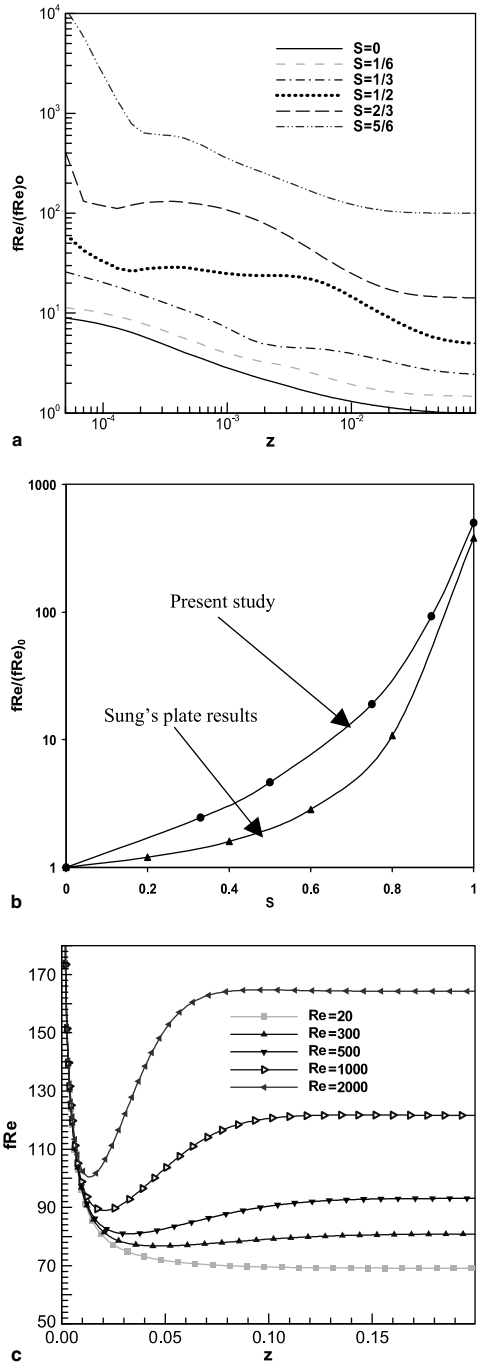

Fig. 10. (a) $fRe/(fRe)_0$ along axial direction, $Re = 100$, $Da = 10^{-5}$. (b) Pressure drop ratio $fRe/(fRe)_0$, $Re = 100$, $Da = 10^{-5}$. (c) fRe variation along axial direction with different Re.

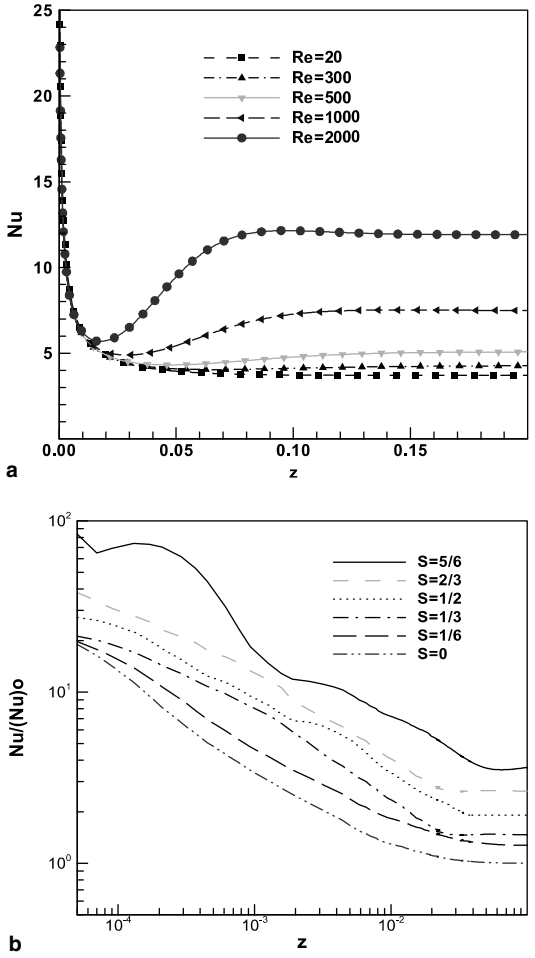

Fig. 11. (a) Nu variation along axial direction with different Re. (b) Nu/Nu_0 Number variation along axial direction, $Re = 100$, $Da = 10^{-5}$.

clear bumps in the curves, in particular for the porous ratio greater than 1/2. This is because the existence and disappearance of the strong counter-rotating secondary flow vortices in the channel. It is also worth noting that since the axial velocity in the porous layer is very small except in the very early entrance region, it is reasonable to simply treat the contribution of the heat transfer is from the convection effect on the fluid layer region plus the conduction effect on the porous media layer of the square channel. Since the Darcy number is relatively small, the heat convection in the porous layer is nearly negligible. Now, if the effective heat conductivity of the porous medium is large enough, the heat transfer at the interface of the porous media layer/liquid layer can be consider as a thick "wall" conduction heat transfer condition. With the porous ratio increase, the aspect ratio of the fluid layer decreases, Nusselt number increases. The Nusselt numbers between a rectangular channel and a fluid layer channel with the same aspect ratio are compared against each other, the Nusselt number of semi-porous channel is higher than that of

a relative rectangular channel (not shown). For instance, when the porous ratio equals 0.5, the fluid layer aspect ratio is 0.5, the Nusselt number is 3.807 in the thermally fully developed region; the Nusselt number for a rectangular channel with 0.5 aspect ratio is 3.391. The additional effect of heat transfer comes from the porous layer.

6. Conclusion

A three-dimensional model was developed for the analysis of the fluid flow and heat transfer in a square channel partially filled with porous medium. The governing Navier–Stokes equations for fluid layer, and volume-averaged Navier–Stokes equations for porous medium layer, were solved using the vorticity–velocity method with power law scheme. The development of velocity fields, temperature distributions, the variations of the friction factor and Nusselt number are presented. It is observed that there exists one pair of strong counter-rotating secondary flow vortices in the channel cross-section in the entrance flow region. This is due to the flow blowing effect of the porous layer. These vortices greatly alter the axial velocity profiles and the temperature distributions in the composite square channel. It is also found that as the porous ratio, S, increases, the flow velocity in fluid layer is increased, and friction factor and Nusselt Number are also increased.

Acknowledgement

The authors would like to thank the National Science Foundation (through NSF-GOALI DMII-9908324), and UW System Applied Research Award for their financial support of the project.

References

[1] B.J. Crowe, Fuel Cells: A Survey, NASA Rep. (SP-5115), Washington, DC, 1973.
[2] K.B. Prater, Polymer electrolyte fuel-cells—a review of recent developments, Power Sources 51 (1994) 129–144.
[3] R. Bradean, K. Promislow, B. Wetton, Transport phenomena in the porous cathode of a proton exchange membrane fuel cell, Numer. Heat Transfer. Part A: Appl. 42 (2002) 121–138.
[4] J. Yuan, M. Rokni, B. Sundén, A numerical investigation of gas flow and heat transfer in proton exchange membrane fuel cells, Numer. Heat Transfer. Part A: Appl. 44 (2003) 255–280.
[5] S.H. Clark, W.M. Kays, Laminar flow forced convection in rectangular tubes, Trans. ASME 75 (1953) 859–866.
[6] J.B. Miles, J.S. Shih, Reconsideration of Nusselt number for laminar fully developed flow in rectangular ducts, Mech. Eng. Dep., University of Missouri, Columbia, 1967, unpublished paper.
[7] F.W. Schmidt, M.E. Newell, Heat transfer in fully developed laminar flow through rectangular and isosceles triangular ducts, Int. J. Heat Mass Transfer 10 (1967) 1121–1123.
[8] G.J. Hwang, F.C. Chou, Effect of wall conduction on combined free and forced laminar convection in horizontal rectangular channels, ASME J. Heat Transfer 109 (1987) 936–942.
[9] S.M. Morcos, A.E. Bergles, Experimental investigation of combined forced and free laminar convection in horizontal tubes, ASME J. Heat Transfer 97 (1975) 212–219.
[10] F.C. Chou, G.J. Hwang, Experiments on combined free and forced laminar convection in horizontal square channels, ASME-JSME Thermal Engineering Joint Conference, Honolulu, HI, 1987, pp. 135–141.
[11] C. Beckmann, R. Viskanta, S. Ramadhyani, Natural convection in vertical enclosures containing simultaneously fluid and porous layers, J. Fluid Mech. 186 (1988) 257–284.
[12] P. Cheng, Heat transfer in geothermal system, Adv. Heat Transfer 14 (1978) 1–105.
[13] Z.V. Stosic, V.D. Stevanovic, Advanced three-dimensional two-fluid porous media method for transient two-phase flow thermal-hydraulics in complex geometries, Numer. Heat Transfer. Part B: Fundam. 41 (2002) 263–289.
[14] P. Jiang, Numerical simulation of forced convection heat transfer in porous plate channels using thermal equilibrium and nonisothermal equilibrium models, Numer. Heat Transfer. Part A: Appl. 35 (1999) 99–113.
[15] G.B. Kim, J.M. Hyun, H.S. Kwak, Buoyant convection in a square cavity partially filled with a heat-generating porous medium, Numer. Heat Transfer. Part A: Appl. 40 (2001) 601–618.
[16] G. Laschet, S. Rex, D. Bohn, N. Moritz, 3-D conjugate analysis of cooled coated plates and homogenization of their thermal properties, Numer. Heat Transfer. Part A: Appl. 42 (2002) 91–106.
[17] R. Bennacer, H. Beji, F. Oueslati, A. Belghith, Multiple natural convection solution in porous media under cross temperature and concentration gradients, Numer. Heat Transfer. Part A: Appl. 39 (2001) 553–567.
[18] G.S. Beavers, D.D. Joseph, Boundary conditions at a naturally permeable wall, J. Fluid Mech. 30 (1967) 197–207.
[19] K. Vafai, R. Thiyagaraja, Analysis of flow and heat transfer at the interface region of a porous medium, Int. J. Heat Mass Transfer 30 (1987) 1391–1405.
[20] K. Vafai, S.J. Kim, Analysis of surface enhancement by a porous substrate, ASME J. Heat Transfer 112 (1990) 700–706.
[21] J.A. Ochoa-Tapaia, S. Whitaker, Momentum jump condition at the boundary between a porous medium and a homogeneous fluid: inertial effects, J. Porous Media 1 (1998) 201–217.
[22] J.A. Ochoa-Tapaia, S. Whitaker, Heat transfer at the boundary between a porous medium and a homogeneous fluid: the one equation model, J. Porous Media 1 (1998) 31–46.
[23] B. Alazmi, K. Vafai, Analysis of fluid flow and heat transfer interfacial conditions between a porous medium

and a fluid layer, Int. J. Heat Mass Transfer 44 (2001) 1735–1749.
[24] C. Bechermann, S. Ramadhyani, R. Viskanta, Natural convection flow and heat transfer between a fluid layer and a porous layer inside a rectangular enclosure, ASME J. Heat Transfer 109 (1987) 363–370.
[25] D. Poulikakos, Buoyancy-driven convection in a horizontal fluid layer extending over a porous substrate, Phys. Fluids 29 (1986) 3949–3957.
[26] Y. Li, Q. Zhu, A model of coupled liquid moisture and heat transfer in porous textiles with consideration of gravity, Numer. Heat Transfer. Part A: Appl. 43 (2003) 501–523.
[27] R.V. Mohan, N.D. Ngo, K.K. Tamma, Three-dimensional resin transfer molding: isothermal process modeling and explicit tracking of moving fronts for thick geometrically complex composites manufacturing applications-part 1, Numer. Heat Transfer. Part A: Appl. 35 (1999) 815–838.
[28] R.V. Mohan, N.D. Ngo, K.K. Tamma, Three-dimensional resin transfer molding: isothermal process modeling and explicit tracking of moving fronts for thick geometrically complex composites manufacturing applications-part 2, Numer. Heat Transfer. Part A: Appl. 35 (1999) 839–858.
[29] G. Croce, H. Beaugendre, W.G. Habashi, Numerical simulation of heat transfer in mist flow, Numer. Heat Transfer. Part A: Appl. 42 (2002) 139–152.
[30] S.B. Sathe, W.Q. Lin, T.W. Tong, Natural convection in enclosures containing an insulation with a permeable fluid-porous interface, Int. J. Heat Fluid Flow 9 (1988) 389–395.
[31] T.C. Jen, A.S. Lavine, G.J. Hwang, Simultaneously developing laminar convection in isothermal square channels, Int. J. Heat Mass Transfer 35 (1) (1992) 239–254.
[32] S.V. Patankar, D.B. Spalding, A calculation procedure for heat, mass and momentum transfer in three-dimensional parabolic flows, Int. J. Heat Mass Transfer 15 (1972) 1787–1806.
[33] G. Dagan, Flow and Transport in Porous Formations, Springer-Verlag, Berlin, 1989.
[34] B. Farouk, T. Fusegi, Predictions of fluid and heat transfer problems by the vorticity–velocity formulation of the Navier–Stokes equations, J. Comput. Phys. 65 (1986) 227–243.
[35] P. Orlandi, Vorticity–velocity formulation for high *Re* flows, Computers Fluids 15 (1987) 137–149.
[36] F.C. Chou, G.J. Hwang, Vorticity–velocity method for the Graetz problem and the effect of natural convection in a horizontal rectangular channel with uniform wall heat flux, ASME J. Heal Transfer 109 (1987) 704–710.
[37] T.C. Jen, A.S. Lavine, Laminar heat transfer and fluid flow in the entrance region of a rotating duct with rectangular cross section: the effect of aspect ratio, ASME J. Heat Transfer 114 (August) (1992) 574–581.
[38] S.V. Patankar, Numerical Heat Transfer and Fluid Flow, Hemisphere, Washington, DC, 1980.
[39] R.H. Shah, A.L. London, Laminar Flow Forced Convection in Ducts, Academic Press, New York, 1978.
[40] T.W. Tong, M.C. Sharatchandra, Heat transfer enhancement using porous inserts, Heat Transfer Flow Porous Media, HTD 156 (1990) 41–46.
[41] H.J. Sung, S.Y. Kim, J.M. Hyun, Forced convection from an isolated heat source in a channel with porous medium, Int. J. Heat Fluid Flow 16 (1995) 527–535.
[42] J. Davalath, Y. Bayazitoglu, Forced convection cooling across rectangular blocks, J. Heat Transfer 109 (1987) 321–327.
[43] P.C. Hwang, K. Vafai, Analysis of forced convection enhancement in a channel using porous blocks, J. Thermophys. Heat Transfer 8 (1994) 563–573.
[44] C.G. Speziale, Analytical methods for the development of Reynolds-stress closures in turbulence, Annu. Rev. Fluid Mech. 23 (1991) 107–157.
[45] J.E. Hart, Instability and secondary flow motion in rotating channel flow, J. Fluid Mech. 45 (2) (1971) 341–351.
[46] E.M. Smirnov, Asymptotic drag formula for the rapidly rotating radial channels of rectangular cross section, Izv. Akad. Nauk. SSSR, Mekh. Zhidk. Gaza (6) (1978) 42–49.